NANO LETTERS
Letter
Cite This: Nano Lett. 2018, 18, 2772−2779
pubs.acs.org/NanoLett

Cation Dynamics Governed Thermal Properties of Lead Halide Perovskite Nanowires

Yuxi Wang,[†,§] Renxing Lin,[†,§] Pengchen Zhu,[†,§] Qinghui Zheng,[†] Qianjin Wang,[†] Deyu Li,[*,‡] and Jia Zhu[*,†]

[†]National Laboratory of Solid State Microstructures, College of Engineering and Applied Sciences, and Collaborative Innovation Center of Advanced Microstructures, Nanjing University, Nanjing 210093, People's Republic of China

[‡]Department of Mechanical Engineering, Vanderbilt University, Nashville, Tennessee 37212, United States

Supporting Information

ABSTRACT: Metal halide perovskite (MHP) nanowires such as hybrid organic−inorganic $CH_3NH_3PbX_3$ (X = Cl, Br, I) have drawn significant attention as promising building blocks for high-performance solar cells, light-emitting devices, and semiconductor lasers. However, the physics of thermal transport in MHP nanowires is still elusive even though it is highly relevant to the device thermal stability and optoelectronic performance. Through combined experimental measurements and theoretical analyses, here we disclose the underlying mechanisms governing thermal transport in three different kinds of lead halide perovskite nanowires ($CH_3NH_3PbI_3$, $CH_3NH_3PbBr_3$ and $CsPbBr_3$). It is shown that the thermal conductivity of $CH_3NH_3PbBr_3$ nanowires is significantly suppressed as compared to that of $CsPbBr_3$ nanowires, which is attributed to the cation dynamic disorder. Furthermore, we observed different temperature-dependent thermal conductivities of hybrid perovskites $CH_3NH_3PbBr_3$ and $CH_3NH_3PbI_3$, which can be attributed to accelerated cation dynamics in $CH_3NH_3PbBr_3$ at low temperature and the combined effects of lower phonon group velocity and higher Umklapp scattering rate in $CH_3NH_3PbI_3$ at high temperature. These data and understanding should shed light on the design of high-performance MHP based thermal and optoelectronic devices.

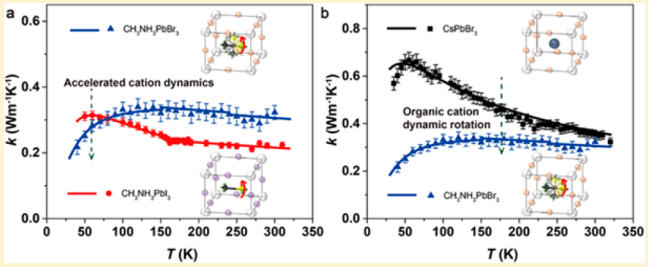

KEYWORDS: *Perovskite, nanowires, cation dynamics, thermal conductivity*

Metal halide perovskites (MHP), as emerging functional materials with tunable compositions and properties, have shown great potential in optoelectronics, such as highly efficient solar cells,[1−5] narrow half-width and wide color-range light-emitting diodes,[6−8] and high Q-factor lasers.[9−13] Whereas nanowires have demonstrated advantages in these optoelectronic applications,[9,10,14−21] thermal stability is a concern that needs to be addressed,[22] as large amount of accumulated heat during device operations will result in various issues including thermomechanical failures and thermochemical degradation.[23,24] In addition, perovskite materials have also been considered as promising for thermoelectrics due to the high Seebeck coefficient and low thermal conductivity.[25−27] Therefore, it is of great importance to understand the thermal properties of MHP nanostructures.

Both theoretical and experimental studies have been carried out to understand the thermal properties of this material family. For example, molecular dynamics modeling[28−30] revealed the effects of phase transition on thermal conductivity of $CH_3NH_3PbI_3$; and the thermal conductivities of bulk single- or polycrystalline $CH_3NH_3PbI_3$, polycrystalline $CH_3NH_3PbI_3$ thin films,[31−34] as well as all-inorganic halide perovskite wires[35] have been experimentally explored.

Here, we systematically investigate the temperature-dependent thermal conductivity of three different kinds of single crystalline perovskite nanowires in the temperature range of 35 to 320 K. The obtained room-temperature thermal conductivity values of $CH_3NH_3PbI_3$, $CH_3NH_3PbBr_3$, and $CsPbBr_3$ nanowires are 0.22, 0.32, and 0.36 W m^{-1} K^{-1}, respectively, which are considerably lower than those of semiconductor nanowires[36,37] and traditional oxide perovskites.[38] Importantly, the very different temperature dependence of the thermal conductivity reveals the critical role of cation dynamics on thermal transport of halide perovskite nanowires.

Single crystalline $CH_3NH_3PbBr_3$, $CsPbBr_3$, and $CH_3NH_3PbI_3$ nanowires were synthesized by solution processed growth techniques (details in Methods). The structures of these three perovskites are illustrated in Figure 1a. Figure 1b−d shows the optical microscopy images of typical as-synthesized perovskite nanowires. The X-ray diffraction (XRD) patterns (Figure 1h) taken from as-synthesized nanowires confirm the cubic phase of $CH_3NH_3PbBr_3$, the

Received: October 17, 2017
Revised: April 1, 2018
Published: April 4, 2018

Downloaded via NANJING UNIV on June 19, 2018 at 14:07:06 (UTC).
See https://pubs.acs.org/sharingguidelines for options on how to legitimately share published articles.

© 2018 American Chemical Society

DOI: 10.1021/acs.nanolett.7b04437
Nano Lett. 2018, 18, 2772−2779

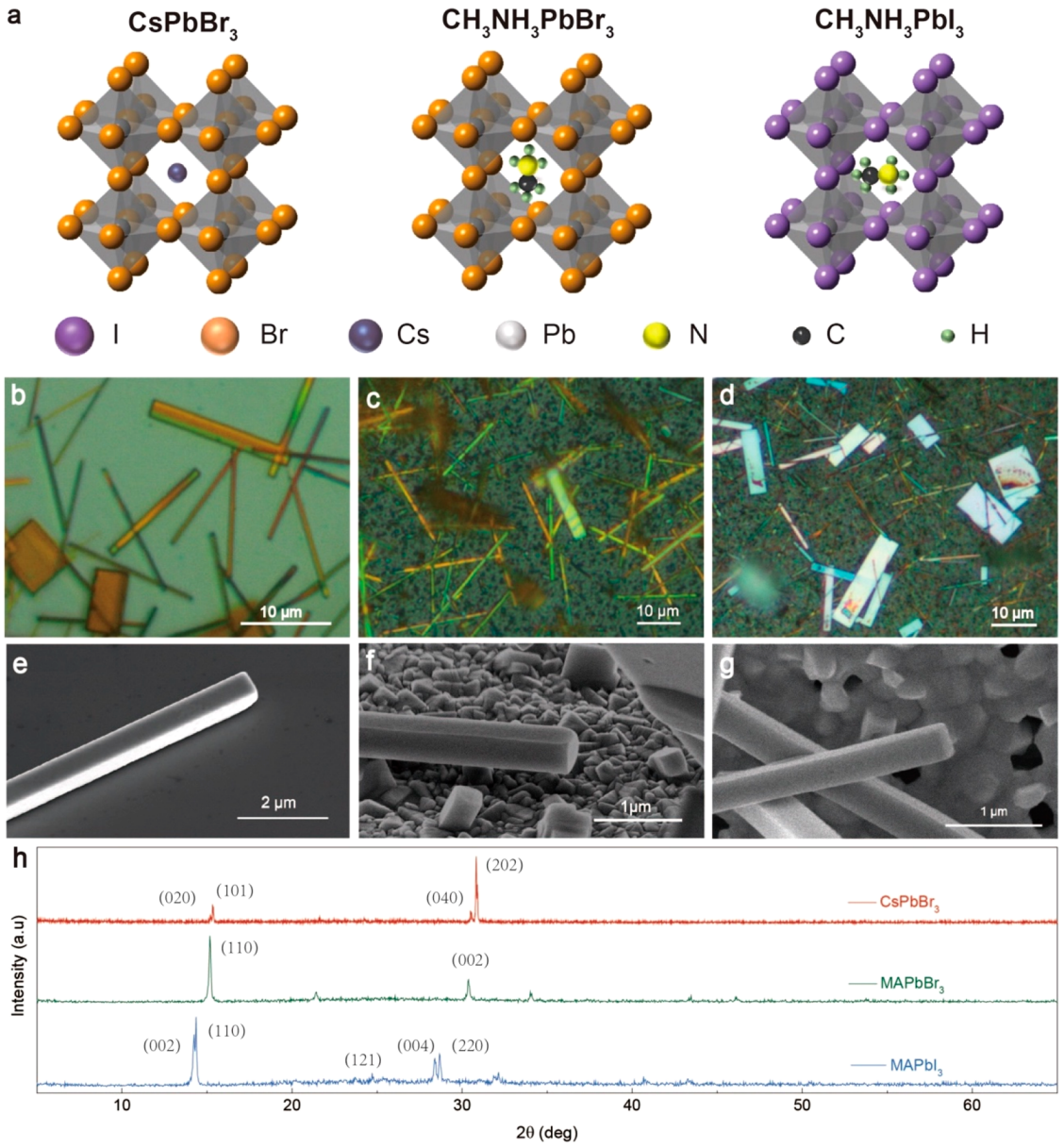

Figure 1. Schematic of three kinds of perovskites and characterizations of single-crystal perovskite nanowires. (a) Schematic of the cage structures of $CsPbBr_3$, $CH_3NH_3PbBr_3$, and $CH_3NH_3PbI_3$ perovskites with the Cs atom in all-inorganic perovskite and methylammonium (MA) cation in hybrid perovskite. The color balls below indicate different atoms. (b–d) Optical microscopy images of as-growth $CsPbBr_3$, $CH_3NH_3PbBr_3$, and $CH_3NH_3PbI_3$, respectively, on FTO glasses. (e–g) Magnified SEM image of nanowires of $CsPbBr_3$, $CH_3NH_3PbBr_3$ and $CH_3NH_3PbI_3$, respectively. The well-formed facets confirm good sample quality. (h) XRD patterns of as-growth nanowires. Characterized peaks confirm typical phase at room temperature. The split of (004) and (220) peaks in $CH_3NH_3PbI_3$ sample is a strong indication of the tetragonal phase rather than the high-temperature cubic phase. Similarly, the split of (040) and (202) in $CsPbBr_3$ sample confirms the room-temperature orthorhombic phase without impurities.

tetragonal phase of $CH_3NH_3PbI_3$ and the orthorhombic phase of $CsPbBr_3$ at room temperature, which all agrees well with the reported results.[9,10] All nanowires have rectangular cross section and well-formed facets as shown in Figure 1e–g. The selected area electron diffraction patterns confirm single crystalline nature of these nanowires (Figure S2).

The thermal measurement is performed by the well-established microbridge technique,[39] which has been widely used to measure the thermal properties of various nanotubes,[40] nanowires,[36,37] and two-dimensional materials.[41,42] In the measurement, the freshly prepared wire sample (Figure 2a) was placed between two suspended membranes serving as heat source and heat sink and electron beam induced Pt deposition was done at the wire-membrane contacts to minimize the contact thermal resistance (see details in Methods). To evaluate the residual contact thermal resistance, we adopted the following formula[43]

$$R_c = \frac{1}{4} \times \frac{1}{\sqrt{hPkA_c}\tanh\left(\sqrt{\frac{hP}{kA_c}}L_c\right)}$$

where h is the heat transfer coefficient between nanowire and supported Pt electrode, P is the effective lateral width of the contact, A_c is the cross-sectional area of the nanowire, and k is the intrinsic thermal conductivity of the measured samples. The

DOI: 10.1021/acs.nanolett.7b04437
Nano Lett. 2018, 18, 2772–2779

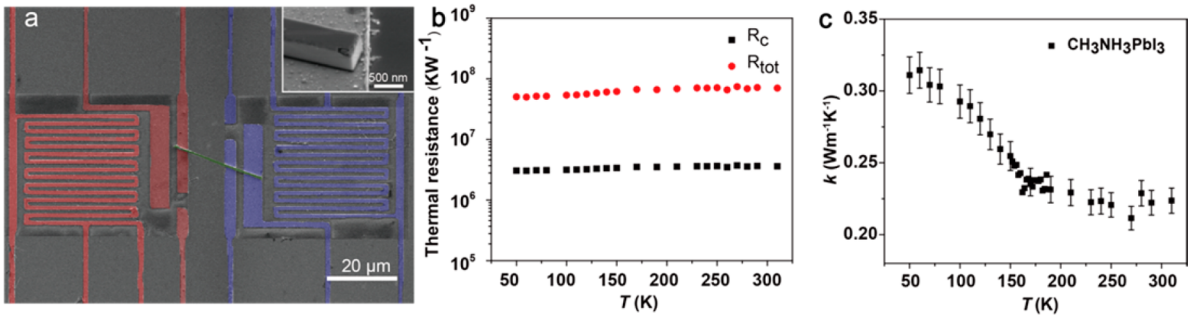

Figure 2. Thermal measurement of perovskite nanowires. (a) False-color SEM image of typical microbridge device with a perovskite nanowire bridging between two suspended pads. The heat flow is defined from heating membrane (red) to sensing membrane (blue) through the nanowire (green). (Inset) High-magnified SEM image of typical measured nanowire. The image shows well-formed facets and a rectangular cross section of long nanowire. (b) Calculated total measured thermal resistance and thermal contact resistance of $CH_3NH_3PbI_3$ nanowire (cross section size: 350 nmx480 nm). The thermal contact resistance account for less than 5% of total thermal resistance. (c) Thermal conductivity of corresponding $CH_3NH_3PbI_3$ nanowire. The dip around 160 K coincides with the orthorhombic-to-tetragonal phase transition.

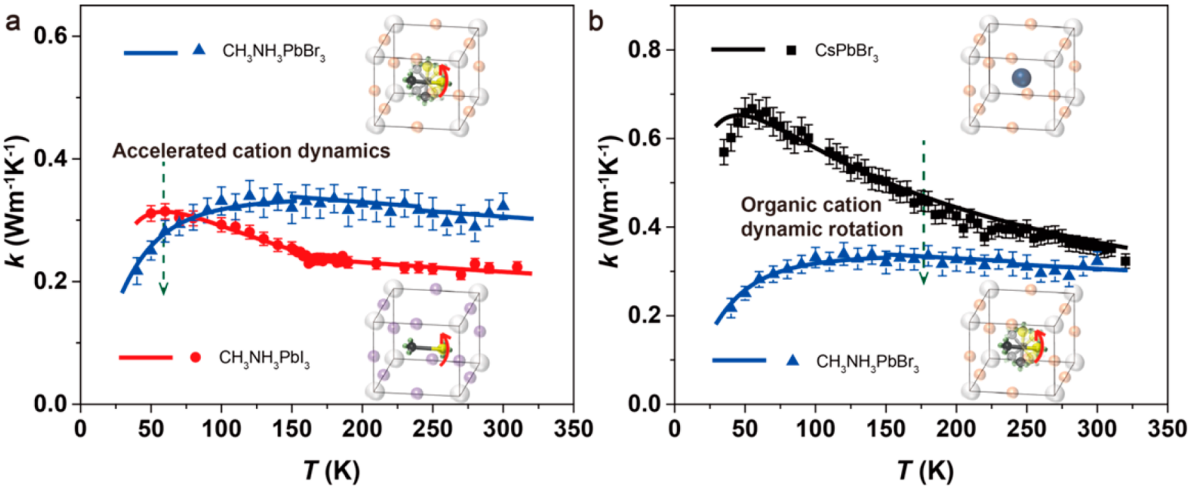

Figure 3. Thermal conductivity of $CsPbBr_3$, $CH_3NH_3PbBr_3$, and $CH_3NH_3PbI_3$ nanowires. (a) Thermal conductivity comparison between $CH_3NH_3PbBr_3$ and $CH_3NH_3PbI_3$ reveals the role of accelerated cation dynamics in suppressing k (green arrow in a) at low temperature. (b) Thermal conductivity comparison between $CsPbBr_3$ and $CH_3NH_3PbBr_3$ reveals the role of cation dynamic in suppressing k (green arrow in b). Insets in (a,b) are the simplified schematic diagrams of $CH_3NH_3PbI_3$, $CH_3NH_3PbBr_3$, and $CsPbBr_3$ unit cell with indication of cation dynamic motion in hybrid perovskite (red arrow in the unit cell). Scattered data points are the measurement results and the solid lines are the model fitting curves. The cross-section sizes for three kinds of nanowires ($CsPbBr_3$, $CH_3NH_3PbBr_3$, and $CH_3NH_3PbI_3$) shown are 320 nm × 390 nm, 200 nm × 340 nm, and 480 nm × 350 nm, respectively.

geometric parameters were carefully determined from scanning electron microscopy (SEM) images (Figure S1), and k was calculated from the measured thermal conductance (G_s). Following the reported procedure,[43] it is confirmed that the calculated contact thermal resistance (Figure 2b) accounts for up to about 5% of the total measured thermal resistance for the $CH_3NH_3PbI_3$ nanowire (details in Supporting Information).

The corresponding thermal conductivity of the same $CH_3NH_3PbI_3$ nanowire is shown in Figure 2c. Similar trend of temperature dependent thermal properties as that of bulk $CH_3NH_3PbI_3$[31,32] is observed. In particular, our data also show a small dip of thermal conductivity at the phase transition temperature around 160 K, consistent with previous work[31] (see zoom-in plot around the phase transition temperature in Figure S4 in the Supporting Information). In addition, the distinct temperature dependence below and above 160 K also indicates the important effect of material phases on the thermal conductivity. Now we focus on the origin of the low thermal conductivity (0.22 W m^{-1} K^{-1} at 300 K). Because the electrical conductivity σ was measured to be merely ~4 S m^{-1} at 300 K, the electronic contribution to the thermal conductivity can be neglected based on the Wiedemann–Franz law, $k_e = L_0\sigma T$, where L_0 is the Lorenz number. As such, the thermal conductivity of the $CH_3NH_3PbI_3$ nanowire is mainly due to lattice vibrations or phonons. For hybrid organic–inorganic $CH_3NH_3PbI_3$, it has been claimed that the low bulk thermal conductivity (0.5 W m^{-1} K^{-1} at room temperature) is due to the resonant scattering between the organic methylammonium (MA) cation and the PbI_6 framework,[31,32] similar to the mechanism for thermoelectric materials of caged structures.[44] The underlying mechanism for the low thermal conductivity of MHP can be understood through the related studies of molecular-scale dynamics.[45−52] The phonon modes affected by the dynamic motion of MA cation yield low phonon group velocity[50] and short phonon lifetimes,[53] which contribute to the low thermal conductivity.

As to the lower room temperature thermal conductivity of the measured nanowire (0.22 W m^{-1} K^{-1}) compared to bulk single crystal $CH_3NH_3PbI_3$,[31] we consider the crystal orientation of as-grown nanowires. Although the tetragonal

DOI: 10.1021/acs.nanolett.7b04437
Nano Lett. 2018, 18, 2772−2779

phase with high crystalline quality is confirmed by X-ray diffraction (XRD) patterns, the rectangular cross section of these nanowires is quite different from the normal rhombohexagonal dodecahedrons bulk single crystal $CH_3NH_3PbI_3$.[54,55] In addition, the nanowire in our case have a specific growth direction (⟨100⟩),[10] which is also the direction of heat transfer in the thermal measurement. This is different from the polycrystalline samples and rhombohexagonal dodecahedrons bulk single crystal.[31] This difference could result in anisotropic thermal transport in the $CH_3NH_3PbI_3$,[28] orginating from both crystal orientation of the PbI_6 framework and the corresponding preferred rotational motion of organic cations inside the framework along the heat flow direction. In addition, we calculated the minimum thermal conductivity k_{min} of $CH_3NH_3PbI_3$ disordered crystal using a simplified method developed by Cahill et al.[56] at room temperature, which yields a value of ∼0.11 W m^{-1} K^{-1} at 300 K (Supporting Information Note 2). This value is still lower than the smallest measured thermal conductivity (0.22 W m^{-1} K^{-1}) of our $CH_3NH_3PbI_3$ nanowires.

To systematically investigate the thermal properties of various kinds of lead halide perovskites, we further measured the thermal conductivity of $CH_3NH_3PbBr_3$ and $CsPbBr_3$ nanowires, in comparison with that of $CH_3NH_3PbI_3$ nanowires. Figure 3a,b shows the measurement results, together with the model analysis based on the Debye−Callaway model.[58] The experimental data for these three kinds of nanowires show quite different temperature dependence and the modeling parameters indicate more scattering induced by cation dynamics in $CH_3NH_3PbBr_3$ perovskite at low temperature than $CH_3NH_3PbI_3$ and $CsPbBr_3$.

Through comparing the measured thermal conductivities of $CH_3NH_3PbBr_3$ and $CH_3NH_3PbI_3$ nanowires, we found out that the halide atom plays a significant role in the thermal transport through these nanowires. $CH_3NH_3PbBr_3$ undergoes orthorhombic-to-tetragonal phase transition at 155 K and a tetragonal-to-cubic phase transition at 236 K.[22] In the low temperature regime of less than 150 K, where both $CH_3NH_3PbBr_3$ and $CH_3NH_3PbI_3$ are of orthorhombic phase, the thermal conductivity of $CH_3NH_3PbBr_3$ is comparable to and even lower than that of $CH_3NH_3PbI_3$. However, the thermal conductivity of $CH_3NH_3PbBr_3$ first increases rapidly at low temperature and then decreases slowly, which is different from the much faster decreasing trend in $CH_3NH_3PbI_3$. The peak in the temperature-dependent thermal conductivity of $CH_3NH_3PbBr_3$ appears at a higher temperature than $CH_3NH_3PbI_3$. It indicates that phonon scattering mechanisms other than Umklapp scattering dominate at low temperature in $CH_3NH_3PbBr_3$, and detailed mechanisms for the different temperature dependence of the thermal conductivity will be discussed later.

For the all-inorganic $CsPbBr_3$ nanowire, in the measured temperature range from 35 to 320 K, it maintains an orthorhombic phase.[59] Therefore, the thermal conductivity versus temperature behavior demonstrates a typical trend for single crystalline materials in a monophasic regime (Figure 3b). It is found that the all-inorganic crystalline $CsPbBr_3$ nanowire also held relatively low k of 0.36 W m^{-1} K^{-1} at room temperature. This low k is consistent with recent reports and can be explained by weaker metal-halide bond, local polar fluctuations, or cluster rattling mechanism in all-inorganic lead halide perovskites.[35,60] Furthermore, Figure 3b also shows that $CH_3NH_3PbBr_3$ has lower thermal conductivity than $CsPbBr_3$ in all of its three phases, which indicates that the organic cations help to further suppress the thermal conductivity irrespective of the materials' phase regime.

To understand the underlying mechanism for the different temperature dependence of thermal conductivity in lead halide perovskites, we compare the Debye-model analysis results with the experimental data. We combined multiple phonon scattering mechanisms and expressed the phonon scattering rate through the Matthiessen's rule. Recent studies have demonstrated sub-100 nm mean free paths in lead halide perovskites,[35,61] even at low temperature of ∼50 K. Therefore, the effect due to phonon-boundary scattering should not play a significant role in our measured temperature range because of the rather large characteristic size of the nanowires (∼300 nm). For the all-inorganic $CsPbBr_3$, our model analysis considering boundary scattering, impurity scattering, and Umklapp scattering matched the experimental data well (details in Supporting Information).

In order to analyze thermal conductivity of hybrid perovskites, we further included resonant scattering in the model analysis at low temperature,[32] in which the resonant frequency ω_0 correlates to the dynamic motion of MA cation. From the calculation of resonant scattering rate, $\tau_r^{-1} = C\frac{\omega^2\omega_0^2}{(\omega^2-\omega_0^2)^2}$, we find that the resonant scattering will dominate when phonons with frequencies around ω_0 make major contributions to the thermal conductivity. In hybrid perovskites, the MA cation has rotational motion in caged structures and can interact with the metal−halide sublattice.[45] It is expected that the interactions can lead to resonant bonding between MA cation and metal−halide sublattice. Importantly, it has been observed that the resonant bonding can cause softened phonon modes and strong anharmonic scattering.[57] The resonant scattering usually exists in the structure containing a quasi-localized rattler[62] (MA cation in our case). It can be a dominant scattering mechanism at low temperature and scatter low energy phonons.[63,64]

It is expected that as the halide atom size decreases, larger lattice spacing favors MA cation fluctuations in the caged structure. The modeling results for the low temperature phase provide a higher resonant frequency of $\omega_0 \sim 6.85 \times 10^{12}$ $rads^{-1}$ for $CH_3NH_3PbBr_3$ than 3.56×10^{12} $rads^{-1}$ for $CH_3NH_3PbI_3$, suggesting higher dynamic disorder in $CH_3NH_3PbBr_3$, which leads to lower thermal conductivity in orthorhombic $CH_3NH_3PbBr_3$. In fact, the resonant frequency of different perovskites can be described by a simple model[65] and $\omega_0 \sim \sqrt{k_0/m_0}$, where k_0 represents the stiffness between the MA cation and PbX_6 cage and m_0 is the mass of MA cation. As the hydrogen bond between the MA cation and PbX_6 cage strengthens from I-based perovskites to Br-based perovskites, it can be imagined that $CH_3NH_3PbBr_3$ has a higher k_0 and therefore a higher ω_0, an indication of the accelerated cation dynamics at low-temperature orthorhombic phase of $CH_3NH_3PbBr_3$. This analysis also suggests that the MA cation dynamics is not fully frozen even at low-temperature phase, which is consistent with the previous observation via neutron spectroscopy.[66] In addition, by comparison of the model parameter B at low-temperature phases, we find $B \sim 7.95 \times 10^{-17}$ s K^{-1} for orthorhombic phase $CH_3NH_3PbI_3$, which is about 10-fold of that of orthorhombic phase $CH_3NH_3PbBr_3$. This suggests the much more dominant role of Umklapp scattering in $CH_3NH_3PbI_3$ than in $CH_3NH_3PbBr_3$ at low-temperature phase.

DOI: 10.1021/acs.nanolett.7b04437
Nano Lett. 2018, 18, 2772−2779

As temperature increases beyond 155 K, the $CH_3NH_3PbBr_3$ changes from orthorhombic phase into tetragonal phase, leading to a different trend of temperature dependence of the thermal conductivity. Instead of resonant scattering, phonon-impurity scattering and Umklapp scattering collectively result in a slowly decreasing trend in high temperature phase in $CH_3NH_3PbBr_3$. A recent theoretical prediction has demonstrated higher k in tetragonal and cubic phase $CH_3NH_3PbBr_3$ than $CH_3NH_3PbI_3$ as a result of higher elastic stiffness.[28] Then the higher thermal conductivity in $CH_3NH_3PbBr_3$ has been attributed to the corresponding higher speed of sound.[61] In addition, it is generally accepted[67] that for larger atomic mass ratio, the gap between acoustic and optic phonon branch is enhanced, which tends to reduce the phonon−phonon scattering rate. This is reflected in the model parameter B, which accounts for the Umklapp scattering rate (details in Supporting Information). We obtained $B \sim 0.52 \times 10^{-17}$ s K^{-1} for tetragonal and cubic phase $CH_3NH_3PbBr_3$, which is lower than that for tetragonal phase $CH_3NH_3PbI_3$, $B \sim 0.84 \times 10^{-17}$ s K^{-1}. Therefore, with the increasing mass ratio between metal and halide atom (from I to Br) in diatomic PbX_6 framework, the thermal conductivity is smaller in $CH_3NH_3PbI_3$ than $CH_3NH_3PbBr_3$ in the tetragonal and cubic phase. As such, while the difference in phonon group velocity could make major contribution to the different thermal conductivity of hybrid perovskites at room temperature, our results suggest that different Umklapp scattering rates could also play a role.

The theoretical model, which explicitly takes into account the contribution of the cation dynamic disorders induced by the organic MA cations in $CH_3NH_3PbBr_3$ and $CH_3NH_3PbI_3$ (Supporting Information Note 1), matches the experimental data very well. The difference of the temperature-dependent thermal conductivity at low temperature between the two hybrid perovskites can be explained by the modeling results. Because of the dominant resonant scattering at low temperature as well as larger speed of sound and lower Umklapp scattering rate at high temperature in $CH_3NH_3PbBr_3$ mentioned above, a crossover could be expected to occur in the midtemperature region, about 70 K in our results. Meanwhile, the cation dynamics helps suppressing thermal conductivity in hybrid perovskites than all-inorganic perovskites (Figure 3b). In addition, the difference of the temperature-dependent thermal conductivity in $CH_3NH_3PbBr_3$ and $CH_3NH_3PbI_3$ might allow tuning of thermal transport through the anion exchange conversion technique in hybrid $CH_3NH_3PbX_3$ (X = I, Br) perovskite nanostructures.[68]

In summary, we systematically studied the temperature-dependent thermal conductivity of hybrid organic−inorganic $CH_3NH_3PbI_3$, $CH_3NH_3PbBr_3$, and all-inorganic $CsPbBr_3$ nanowires, revealing the combined effects of organic cations and halide anions on the thermal properties of perovskites. Importantly, we take it a step further by correlating the MA cation dynamics mechanism[45,53] to thermal transport in these materials through demonstrating that accelerated cation dynamics is associated with decreasing halide atom size. These discoveries reveal the intriguing thermal properties in lead halide perovskites, which can serve as guidelines for developing MHP based optoelectronic devices. In addition, it provides opportunities for applications in thermal management and thermal energy storage and conversion, like thermoelectricity, given the discovered ultralow thermal conductivity,[31,69] tunable electrical properties,[70,71] and potential high Seebeck coefficient[72,73] of these MHPs.

Methods. *Sample Preparation.* $CH_3NH_3PbI_3$ and $CH_3NH_3PbBr_3$ were synthesized following previous literatures.[10] To obtain high quality samples, we made several improvements. The solution of 100 mg/mL $Pb(Ac)_2$ in deionized water was dropped on the FTO glass kept at 75 °C. After partial evaporation of the solvent due to the heating, the $Pb(Ac)_2$ solution became concentrated and sticky and then we spun the substrate. The as-formed $Pb(Ac)_2$ film was dried at 75 °C on a hot plate for another 1 h. Then we immersed the $Pb(Ac)_2$ FTO glass side on 40 mg/mL CH_3NH_3I or 4 mg/mL CH_3NH_3Br/isopropanol solution for 16 h at room temperature to form the desired $CH_3NH_3PbI_3$ or $CH_3NH_3PbBr_3$ nanowires.

To synthesize $CsPbBr_3$ nanowires, 0.05 M CsBr and 0.05 M $PbBr_2$ were first dissolved in DMSO. Then chlorobenzene was dropped into the as-prepared solution in 4:1 volume ratio. After a few minutes, some precipitates were formed. We used a dropper to transfer some of the precipitates accompanied by the solution onto a substrate and the $CsPbBr_3$ nanowires would form after evaporation of the solvent.

All samples were stored in a nitrogen-filled glovebox after sample growth and transfer prior to thermal measurements.

Sample Characterization. The optical images were obtained with Eclipse LV100D, Nikon. The SEM images of perovskite nanowires were obtained using Dual-beam FIB 235, FEI Strata. The XRD patterns was characterized on a Rigaku Ultima X-ray IV diffractometer using a Cu K_α 5 deg·min^{-1}.

Thermal Measurements. Thermal conductivity measurements were conducted in a cryostat (Janis CCS-450) under high vacuum (<1 × 10^{-6} mbar). Perovskite nanowires were bridged between two suspended membranes, both of which can serve as thermometer and heater in the thermal measurement, by tungsten probe, and electron beam-induced deposition (EBID) of Pt (Dual-beam FIB 235, FEI Strata 2 kV, 86 pA) was used to minimize the contact thermal resistance. A μA-DC current was used to generate Joule heat (Q_{tot}) on the heating membrane and to induce temperature rise in heating (ΔT_h) and sensing (ΔT_s) membranes, respectively, due to the heat transfer through the nanowire. By carefully analyzing the thermal circuit and determining the heat transfer through the nanowire (Q_2), the thermal conductance of the nanowire can be expressed as $G_s = \frac{Q_{tot}}{\Delta T_h + \Delta T_s} \times \frac{\Delta T_s}{\Delta T_h - \Delta T_s}$. Then, with determination of the nanowire geometry using SEM, the thermal conductivity can be obtained by $k = G_s \frac{l}{w \times h}$, where l, w, and h are the length, width, and thickness of the nanowire, respectively. To reduce the effect of radiative heat transfer,[53] two copper radiation shields were installed into the measurement system with the inner one mounted directly onto the sample holder.

■ ASSOCIATED CONTENT

Supporting Information

The Supporting Information is available free of charge on the ACS Publications website at DOI: 10.1021/acs.nanolett.7b04437.

Additional information regarding thermal measurement results and details about modeling analysis(PDF)

■ AUTHOR INFORMATION

Corresponding Authors

*E-mail: jiazhu@nju.edu.cn (J.Z.).
*E-mail: deyu.li@vanderbilt.edu (D.L.).

DOI: 10.1021/acs.nanolett.7b04437
Nano Lett. 2018, 18, 2772−2779

ORCID

Deyu Li: 0000-0001-8364-0924
Jia Zhu: 0000-0002-2871-4369

Author Contributions

[§]Y.W., R.L., and P.Z. contributed equally to this work.

Notes

The authors declare no competing financial interest.

■ ACKNOWLEDGMENTS

We acknowledge the microfabrication center of National Laboratory of Solid State Microstructures (NLSSM) for technique support. This work is jointly supported by the State Key Program for Basic Research of China (No. 2015CB659300) and the National Key Research and Development Program of China (No. 2017YFA0205700), National Natural Science Foundation of China (No. 11621091, 11574143, 61735008), Natural Science Foundation of Jiangsu Province (No. BK20150056).

■ ABBREVIATIONS

MHP, metal halide perovskite; XRD, X-ray diffraction; MA, methylammonium

■ REFERENCES

(1) Shin, S. S.; Yeom, E. J.; Yang, W. S.; Hur, S.; Kim, M. G.; Im, J.; Seo, J.; Noh, J. H.; Seok, S. I. Colloidally prepared La-doped BaSnO3 electrodes for efficient, photostable perovskite solar cells. *Science* **2017**, *356* (6334), 167−171.

(2) Eperon, G. E.; Leijtens, T.; Bush, K. A.; Prasanna, R.; Green, T.; Wang, J. T.-W.; McMeekin, D. P.; Volonakis, G.; Milot, R. L.; May, R.; Palmstrom, A.; Slotcavage, D. J.; Belisle, R. A.; Patel, J. B.; Parrott, E. S.; Sutton, R. J.; Ma, W.; Moghadam, F.; Conings, B.; Babayigit, A.; Boyen, H.-G.; Bent, S.; Giustino, F.; Herz, L. M.; Johnston, M. B.; McGehee, M. D.; Snaith, H. J. Perovskite-perovskite tandem photovoltaics with optimized band gaps. *Science* **2016**, *354* (6314), 861−865.

(3) Ummadisingu, A.; Steier, L.; Seo, J. Y.; Matsui, T.; Abate, A.; Tress, W.; Gratzel, M. The effect of illumination on the formation of metal halide perovskite films. *Nature* **2017**, *545* (7653), 208−212.

(4) Lee, J. W.; Kim, S. G.; Bae, S. H.; Lee, D. K.; Lin, O.; Yang, Y.; Park, N. G. The Interplay between Trap Density and Hysteresis in Planar Heterojunction Perovskite Solar Cells. *Nano Lett.* **2017**, *17* (7), 4270−4276.

(5) Ke, W.; Stoumpos, C. C.; Logsdon, J. L.; Wasielewski, M. R.; Yan, Y.; Fang, G.; Kanatzidis, M. G. TiO2−ZnS Cascade Electron Transport Layer for Efficient Formamidinium Tin Iodide Perovskite Solar Cells. *J. Am. Chem. Soc.* **2016**, *138* (45), 14998−15003.

(6) Wang, N.; Cheng, L.; Ge, R.; Zhang, S.; Miao, Y.; Zou, W.; Yi, C.; Sun, Y.; Cao, Y.; Yang, R.; Wei, Y.; Guo, Q.; Ke, Y.; Yu, M.; Jin, Y.; Liu, Y.; Ding, Q.; Di, D.; Yang, L.; Xing, G.; Tian, H.; Jin, C.; Gao, F.; Friend, R. H.; Wang, J.; Huang, W. Perovskite light-emitting diodes based on solution- processed self-organized multiple quantum wells. *Nat. Photonics* **2016**, *10* (11), 699−704.

(7) Yuan, M.; Quan, L. N.; Comin, R.; Walters, G.; Sabatini, R.; Voznyy, O.; Hoogland, S.; Zhao, Y.; Beauregard, E. M.; Kanjanaboos, P.; Lu, Z.; Kim, D. H.; Sargent, E. H. Perovskite energy funnels for efficient light-emitting diodes. *Nat. Nanotechnol.* **2016**, *11* (10), 872−877.

(8) Cho, H.; Jeong, S.-H.; Park, M.-H.; Kim, Y.-H.; Wolf, C.; Lee, C.-L.; Heo, J. H.; Sadhanala, A.; Myoung, N.; Yoo, S.; Im, S. H.; Friend, R. H.; Lee, T.-W. Overcoming the electroluminescence efficiency limitations of perovskite light-emitting diodes. *Science* **2015**, *350* (6265), 1222−1225.

(9) Eaton, S. W.; Lai, M.; Gibson, N. A.; Wong, A. B.; Dou, L.; Ma, J.; Wang, L. W.; Leone, S. R.; Yang, P. Lasing in robust cesium lead halide perovskite nanowires. *Proc. Natl. Acad. Sci. U. S. A.* **2016**, *113* (8), 1993−8.

(10) Zhu, H.; Fu, Y.; Meng, F.; Wu, X.; Gong, Z.; Ding, Q.; Gustafsson, M. V.; Trinh, M. T.; Jin, S.; Zhu, X. Y. Lead halide perovskite nanowire lasers with low lasing thresholds and high quality factors. *Nat. Mater.* **2015**, *14* (6), 636−42.

(11) Green, M. A.; Ho-Baillie, A.; Snaith, H. J. The emergence of perovskite solar cells. *Nat. Photonics* **2014**, *8* (7), 506−514.

(12) Stranks, S. D.; Snaith, H. J. Metal-halide perovskites for photovoltaic and light-emitting devices. *Nat. Nanotechnol.* **2015**, *10* (5), 391−402.

(13) Sutherland, B. R.; Sargent, E. H. Perovskite photonic sources. *Nat. Photonics* **2016**, *10* (5), 295−302.

(14) Fu, Y.; Meng, F.; Rowley, M. B.; Thompson, B. J.; Shearer, M. J.; Ma, D.; Hamers, R. J.; Wright, J. C.; Jin, S. Solution Growth of Single Crystal Methylammonium Lead Halide Perovskite Nanostructures for Optoelectronic and Photovoltaic Applications. *J. Am. Chem. Soc.* **2015**, *137* (17), 5810−8.

(15) Zhu, P.; Gu, S.; Shen, X.; Xu, N.; Tan, Y.; Zhuang, S.; Deng, Y.; Lu, Z.; Wang, Z.; Zhu, J. Direct Conversion of Perovskite Thin Films into Nanowires with Kinetic Control for Flexible Optoelectronic Devices. *Nano Lett.* **2016**, *16* (2), 871−6.

(16) Fu, Y.; Zhu, H.; Schrader, A. W.; Liang, D.; Ding, Q.; Joshi, P.; Hwang, L.; Zhu, X. Y.; Jin, S. Nanowire Lasers of Formamidinium Lead Halide Perovskites and Their Stabilized Alloys with Improved Stability. *Nano Lett.* **2016**, *16* (2), 1000−8.

(17) Xiao, R.; Hou, Y.; Fu, Y.; Peng, X.; Wang, Q.; Gonzalez, E.; Jin, S.; Yu, D. Photocurrent Mapping in Single-Crystal Methylammonium Lead Iodide Perovskite Nanostructures. *Nano Lett.* **2016**, *16* (12), 7710−7717.

(18) Fu, Y.; Zhu, H.; Stoumpos, C. C.; Ding, Q.; Wang, J.; Kanatzidis, M. G.; Zhu, X.; Jin, S. Broad Wavelength Tunable Robust Lasing from Single-Crystal Nanowires of Cesium Lead Halide Perovskites (CsPbX3, X = Cl, Br, I). *ACS Nano* **2016**, *10* (8), 7963−72.

(19) Chen, J.; Fu, Y.; Samad, L.; Dang, L.; Zhao, Y.; Shen, S.; Guo, L.; Jin, S. Vapor-Phase Epitaxial Growth of Aligned Nanowire Networks of Cesium Lead Halide Perovskites (CsPbX3, X = Cl, Br, I). *Nano Lett.* **2017**, *17* (1), 460−466.

(20) Xing, J.; Liu, X. F.; Zhang, Q.; Ha, S. T.; Yuan, Y. W.; Shen, C.; Sum, T. C.; Xiong, Q. Vapor Phase Synthesis of Organometal Halide Perovskite Nanowires for Tunable Room-Temperature Nanolasers. *Nano Lett.* **2015**, *15* (7), 4571−7.

(21) Im, J. H.; Luo, J.; Franckevicius, M.; Pellet, N.; Gao, P.; Moehl, T.; Zakeeruddin, S. M.; Nazeeruddin, M. K.; Gratzel, M.; Park, N. G. Nanowire Perovskite Solar Cell. *Nano Lett.* **2015**, *15* (3), 2120−6.

(22) Leijtens, T.; Eperon, G. E.; Noel, N. K.; Habisreutinger, S. N.; Petrozza, A.; Snaith, H. J. Stability of Metal Halide Perovskite Solar Cells. *Adv. Energy Mater.* **2015**, *5* (20), 1500963.

(23) Pop, E. Energy Dissipation and Transport in Nanoscale Devices. *Nano Res.* **2010**, *3* (3), 147−169.

(24) Moore, A. L.; Shi, L. Emerging Challenges and Materials for Thermal Management of Electronics. *Mater. Today* **2014**, *17* (4), 163−174.

(25) He, Y.; Galli, G. Perovskites for Solar Thermoelectric Applications: A First Principle Study of $CH_3NH_3AI_3$ (A = Pb and Sn). *Chem. Mater.* **2014**, *26* (18), 5394−5400.

(26) Mettan, X.; Pisoni, R.; Matus, P.; Pisoni, A.; Jaćimović, J.; Náfrádi, B.; Spina, M.; Pavuna, D.; Forró, L.; Horváth, E. Tuning of the Thermoelectric Figure of Merit of Ch3nh3mi3(M═Pb,Sn) Photovoltaic Perovskites. *J. Phys. Chem. C* **2015**, *119* (21), 11506−11510.

(27) Filippetti, A.; Caddeo, C.; Delugas, P.; Mattoni, A. Appealing Perspectives of Hybrid Lead−Iodide Perovskites as Thermoelectric Materials. *J. Phys. Chem. C* **2016**, *120* (50), 28472−28479.

(28) Wang, M.; Lin, S. Anisotropic and Ultralow Phonon Thermal Transport in Organic-Inorganic Hybrid Perovskites: Atomistic Insights into Solar Cell Thermal Management and Thermoelectric Energy Conversion Efficiency. *Adv. Funct. Mater.* **2016**, *26* (29), 5297−5306.

DOI: 10.1021/acs.nanolett.7b04437
Nano Lett. 2018, 18, 2772−2779

(29) Caddeo, C.; Melis, C.; Saba, M. I.; Filippetti, A.; Colombo, L.; Mattoni, A. Tuning the Thermal Conductivity of Methylammonium Lead Halide by the Molecular Substructure. *Phys. Chem. Chem. Phys.* **2016**, *18* (35), 24318−24.
(30) Qian, X.; Gu, X.; Yang, R. Lattice thermal conductivity of organic-inorganic hybrid perovskite $CH_3NH_3PbI_3$. *Appl. Phys. Lett.* **2016**, *108* (6), 063902.
(31) Pisoni, A.; Jacimovic, J.; Barisic, O. S.; Spina, M.; Gaal, R.; Forro, L.; Horvath, E. Ultra-Low Thermal Conductivity in Organic−Inorganic Hybrid Perovskite $CH_3NH_3PbI_3$. *J. Phys. Chem. Lett.* **2014**, *5* (14), 2488−92.
(32) Kovalsky, A.; Wang, L.; Marek, G. T.; Burda, C.; Dyck, J. S. Thermal Conductivity of $CH_3NH_3PbI_3$ and $CsPbI_3$: Measuring the Effect of the Methylammonium Ion on Phonon Scattering. *J. Phys. Chem. C* **2017**, *121* (6), 3228−3233.
(33) Chen, Q.; Zhang, C.; Zhu, M.; Liu, S.; Siemens, M. E.; Gu, S.; Zhu, J.; Shen, J.; Wu, X.; Liao, C.; Zhang, J.; Wang, X.; Xiao, M. Efficient Thermal Conductance in Organometallic Perovskite $CH_3NH_3PbI_3$ Films. *Appl. Phys. Lett.* **2016**, *108* (8), 081902.
(34) Guo, Z.; Yoon, S. J.; Manser, J. S.; Kamat, P. V.; Luo, T. Structural Phase- and Degradation-Dependent Thermal Conductivity of $CH_3NH_3PbI_3$ perovskite Thin Films. *J. Phys. Chem. C* **2016**, *120* (12), 6394−6401.
(35) Lee, W.; Li, H.; Wong, A. B.; Zhang, D.; Lai, M.; Yu, Y.; Kong, Q.; Lin, E.; Urban, J. J.; Grossman, J. C.; Yang, P. Ultralow Thermal Conductivity in All-Inorganic Halide Perovskites. *Proc. Natl. Acad. Sci. U. S. A.* **2017**, *114* (33), 8693−8697.
(36) Li, D.; Wu, Y.; Kim, P.; Shi, L.; Yang, P.; Majumdar, A. Thermal Conductivity of Individual Silicon Nanowires. *Appl. Phys. Lett.* **2003**, *83* (14), 2934−2936.
(37) Hochbaum, A. I.; Chen, R.; Delgado, R. D.; Liang, W.; Garnett, E. C.; Najarian, M.; Majumdar, A.; Yang, P. Enhanced Thermoelectric Performance of Rough Silicon Nanowires. *Nature* **2008**, *451* (7175), 163−7.
(38) Yu, C.; Scullin, M. L.; Huijben, M.; Ramesh, R.; Majumdar, A. Thermal Conductivity Reduction in Oxygen-Deficient Strontium Titanates. *Appl. Phys. Lett.* **2008**, *92* (19), 191911.
(39) Shi, L.; Li, D.; Yu, C.; Jang, W.; Kim, D.; Yao, Z.; Kim, P.; Majumdar, A. Measuring Thermal and Thermoelectric Properties of One-Dimensional Nanostructures Using a Microfabricated Device. *J. Heat Transfer* **2003**, *125* (5), 881.
(40) Pettes, M. T.; Shi, L. Thermal and Structural Characterizations of Individual Single-, Double-, and Multi-Walled Carbon Nanotubes. *Adv. Funct. Mater.* **2009**, *19* (24), 3918−3925.
(41) Jo, I.; Pettes, M. T.; Ou, E.; Wu, W.; Shi, L. Basal-Plane Thermal Conductivity of Few-Layer Molybdenum Disulfide. *Appl. Phys. Lett.* **2014**, *104* (20), 201902.
(42) Xu, X.; Pereira, L. F.; Wang, Y.; Wu, J.; Zhang, K.; Zhao, X.; Bae, S.; Tinh Bui, C.; Xie, R.; Thong, J. T.; Hong, B. H.; Loh, K. P.; Donadio, D.; Li, B.; Ozyilmaz, B. Length-dependent thermal conductivity in suspended single-layer graphene. *Nat. Commun.* **2014**, *5*, 3689.
(43) Zhu, J.; Hippalgaonkar, K.; Shen, S.; Wang, K.; Abate, Y.; Lee, S.; Wu, J.; Yin, X.; Majumdar, A.; Zhang, X. Temperature-Gated Thermal Rectifier for Active Heat Flow Control. *Nano Lett.* **2014**, *14* (8), 4867−72.
(44) Zhu, T.; Liu, Y.; Fu, C.; Heremans, J. P.; Snyder, J. G.; Zhao, X. Compromise and Synergy in High-Efficiency Thermoelectric Materials. *Adv. Mater.* **2017**, *29*, 14.
(45) Selig, O.; Sadhanala, A.; Muller, C.; Lovrincic, R.; Chen, Z.; Rezus, Y. L.; Frost, J. M.; Jansen, T. L.; Bakulin, A. A. Organic Cation Rotation and Immobilization in Pure and Mixed Methylammonium Lead-Halide Perovskites. *J. Am. Chem. Soc.* **2017**, *139* (11), 4068−4074.
(46) Mattoni, A.; Filippetti, A.; Saba, M. I.; Caddeo, C.; Delugas, P. Temperature Evolution of Methylammonium Trihalide Vibrations at the Atomic Scale. *J. Phys. Chem. Lett.* **2016**, *7* (3), 529−35.
(47) Zhu, H.; Miyata, K.; Fu, Y.; Wang, J.; Joshi, P. P.; Niesner, D.; Williams, K. W.; Jin, S.; Zhu, X.-Y. Screening in Crystalline Liquids Protects Energetic Carriers in Hybrid Perovskites. *Science* **2016**, *353* (6306), 1409−1413.
(48) Mattoni, A.; Filippetti, A.; Saba, M. I.; Delugas, P. Methylammonium Rotational Dynamics in Lead Halide Perovskite by Classical Molecular Dynamics: The Role of Temperature. *J. Phys. Chem. C* **2015**, *119* (30), 17421−17428.
(49) Leguy, A. M.; Frost, J. M.; McMahon, A. P.; Sakai, V. G.; Kochelmann, W.; Law, C.; Li, X.; Foglia, F.; Walsh, A.; O'Regan, B. C.; Nelson, J.; Cabral, J. T.; Barnes, P. R. The Dynamics of Methylammonium Ions in Hybrid Organic-Inorganic Perovskite Solar Cells. *Nat. Commun.* **2015**, *6*, 7124.
(50) Li, B.; Kawakita, Y.; Liu, Y.; Wang, M.; Matsuura, M.; Shibata, K.; Ohira-Kawamura, S.; Yamada, T.; Lin, S.; Nakajima, K.; Liu, S. F. Polar rotor scattering as atomic-level origin of low mobility and thermal conductivity of perovskite $CH_3NH_3PbI_3$. *Nat. Commun.* **2017**, *8*, 16086.
(51) Hata, T.; Giorgi, G.; Yamashita, K. The Effects of the Organic−Inorganic Interactions on the Thermal Transport Properties of $CH_3NH_3PbI_3$. *Nano Lett.* **2016**, *16* (4), 2749−53.
(52) Ong, W. L.; O'Brien, E. S.; Dougherty, P. S.; Paley, D. W.; Fred Higgs Iii, C.; McGaughey, A. J.; Malen, J. A.; Roy, X. Orientational Order Controls Crystalline and Amorphous Thermal Transport in Superatomic Crystals. *Nat. Mater.* **2017**, *16* (1), 83−88.
(53) Beecher, A. N.; Semonin, O. E.; Skelton, J. M.; Frost, J. M.; Terban, M. W.; Zhai, H.; Alatas, A.; Owen, J. S.; Walsh, A.; Billinge, S. J. L. Direct Observation of Dynamic Symmetry Breaking above Room Temperature in Methylammonium Lead Iodide Perovskite. *ACS Energy Lett.* **2016**, *1* (4), 880−887.
(54) Liu, Y.; Yang, Z.; Cui, D.; Ren, X.; Sun, J.; Liu, X.; Zhang, J.; Wei, Q.; Fan, H.; Yu, F.; Zhang, X.; Zhao, C.; Liu, S. F. Two-Inch-Sized Perovskite $CH_3NH_3PbX_3$ (X = Cl, Br, I) Crystals: Growth and Characterization. *Adv. Mater.* **2015**, *27* (35), 5176−83.
(55) Liu, Y.; Zhang, Y.; Yang, Z.; Yang, D.; Ren, X.; Pang, L.; Liu, S. F. Two-Inch-Sized Perovskite $CH_3NH_3PbX_3$ (X = Cl, Br, I) Crystals: Growth and Characterization. *Adv. Mater.* **2016**, *28* (41), 9204−9209.
(56) Cahill, D. G.; Watson, S. K.; Pohl, R. O. Lower Limit to the Thermal Conductivity of Disordered Crystals. *Phys. Rev. B: Condens. Matter Mater. Phys.* **1992**, *46* (10), 6131−6140.
(57) Lee, S.; Esfarjani, K.; Luo, T.; Zhou, J.; Tian, Z.; Chen, G. Resonant Bonding Leads to Low Lattice Thermal Conductivity. *Nat. Commun.* **2014**, *5*, 3525.
(58) Callaway. Model for Lattice Thermal Conductivity at Low Temperatures. *Phys. Rev.* **1959**, *113* (4), 1046−1051.
(59) Hirotsu, S.; Harada, J.; Iizumi, M.; Gesi, K. Structural Phase Transitions in $CsPbBr_3$. *J. Phys. Soc. Jpn.* **1974**, *37*, 1393−1398.
(60) Yaffe, O.; Guo, Y.; Tan, L. Z.; Egger, D. A.; Hull, T.; Stoumpos, C. C.; Zheng, F.; Heinz, T. F.; Kronik, L.; Kanatzidis, M. G.; Owen, J. S.; Rappe, A. M.; Pimenta, M. A.; Brus, L. E. Local Polar Fluctuations in Lead Halide Perovskite Crystals. *Phys. Rev. Lett.* **2017**, *118* (13), 136001.
(61) Elbaz, G. A.; Ong, W. L.; Doud, E. A.; Kim, P.; Paley, D. W.; Roy, X.; Malen, J. A. Phonon Speed, Not Scattering, Differentiates Thermal Transport in Lead Halide Perovskites. *Nano Lett.* **2017**, *17* (9), 5734−5739.
(62) Pohl, R. O. Thermal Conductivity and Phonon Resonance Scattering. *Phys. Rev. Lett.* **1962**, *8* (12), 481−483.
(63) Sales, B. C.; Chakoumakos, B. C.; Mandrus, D. Thermoelectric Properties of Thallium-Filled Skutterudites. *Phys. Rev. B: Condens. Matter Mater. Phys.* **2000**, *61* (4), 2475−2481.
(64) Holland, M. G. Phonon Scattering in Semiconductors from Thermal Conductivity Studies. *Phys. Rev.* **1964**, *134* (2A), A471−A480.
(65) Toberer, E. S.; Zevalkink, A.; Snyder, G. J. Phonon Engineering through Crystal Chemistry. *J. Mater. Chem.* **2011**, *21* (40), 15843.
(66) Druzbicki, K.; Pinna, R. S.; Rudic, S.; Jura, M.; Gorini, G.; Fernandez-Alonso, F. Unexpected Cation Dynamics in the Low-Temperature Phase of Methylammonium Lead Iodide: The Need for Improved Models. *J. Phys. Chem. Lett.* **2016**, *7* (22), 4701−4709.

DOI: 10.1021/acs.nanolett.7b04437
Nano Lett. 2018, 18, 2772−2779

(67) Chen, G. *Nanoscale energy transport and conversion: a parallel treatment of electrons, molecules, phonons, and photons*; Oxford University Press: Oxford, 2005; p xxiii, 531.
(68) Wong, A. B.; Lai, M.; Eaton, S. W.; Yu, Y.; Lin, E.; Dou, L.; Fu, A.; Yang, P. Growth and Anion Exchange Conversion of $CH_3NH_3PbX_3$ Nanorod Arrays for Light-Emitting Diodes. *Nano Lett.* **2015**, *15* (8), 5519−24.
(69) Shen, C.; Du, W.; Wu, Z.; Xing, J.; Ha, S. T.; Shang, Q.; Xu, W.; Xiong, Q.; Liu, X.; Zhang, Q. Thermal Conductivity of Suspended Single Crystal $CH_3NH_3PbI_3$ Platelets at Room Temperature. *Nanoscale* **2017**, *9* (24), 8281−8287.
(70) Wang, Q.; Shao, Y.; Xie, H.; Lyu, L.; Liu, X.; Gao, Y.; Huang, J. Qualifying composition dependent p and n self-doping in $CH_3NH_3PbI_3$. *Appl. Phys. Lett.* **2014**, *105* (16), 163508.
(71) Noh, J. H.; Im, S. H.; Heo, J. H.; Mandal, T. N.; Seok, S. I. Chemical Management for Colorful, Efficient, and Stable Inorganic-Organic Hybrid Nanostructured Solar Cells. *Nano Lett.* **2013**, *13* (4), 1764−9.
(72) Zhao, T.; Wang, D.; Shuai, Z. Doping Optimization of Organic-Inorganic Hybrid Perovskite $CH_3NH_3PbI_3$ for High Thermoelectric Efficiency. *Synth. Met.* **2017**, *225*, 108−114.
(73) Ye, T.; Wang, X.; Li, X.; Yan, A. Q.; Ramakrishna, S.; Xu, J. Ultra-High Seebeck Coefficient and Low Thermal Conductivity of a Centimeter-Sized Perovskite Single Crystal Acquired by a Modified Fast Growth Method. *J. Mater. Chem. C* **2017**, *5* (5), 1255−1260.

DOI: 10.1021/acs.nanolett.7b04437
Nano Lett. 2018, 18, 2772−2779